ACS SENSORS

pubs.acs.org/acssensors
Article

High-Throughput Human Histone Detection by an Engineered Actinoporin Nanopore

Marija Srnko, Gašper Šolinc, Ana Crnković, Franci Merzel, Michael Jordan, E. Jayne Wallace, Marjetka Podobnik, and Gregor Anderluh*

Cite This: *ACS Sens.* 2026, 11, 2016−2029

ABSTRACT: The use of protein nanopores has proven to be very promising for the identification of proteins or the sequencing of peptides. However, their widespread use in biosensor applications is limited by more complex molecular properties of proteins in comparison to nucleic acids. Here, we developed an α-helical Fav nanopore from the coral *Orbicella faveolata* to detect human histones using a commercial MinION device. The engineered nanopores showed stable insertion into the polymeric membrane support. Bulk analysis of several tens to hundreds of pores per measurement revealed significant differences in mean current passing the pore and current noise resulting from capturing different full-length human histones or their post-translationally modified variants into the pore lumen. Importantly, detailed blocking analyses confirmed histone-specific signals that allow further discrimination between two medically important extracellular histones in mixtures. The newly developed Fav nanopore and high-throughput approach for the detection of biomedically important proteins is an important step towards the widespread use of nanopores in modern analytics.

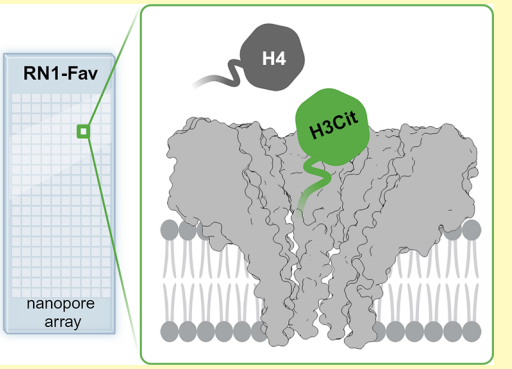

KEYWORDS: *nanopores, actinoporins, histones, biomarkers, sensors*

Nanopore sensing is a fast, real-time, and cost-effective technology that can detect a wide range of analytes in a high-throughput manner. It is a rapidly developing tool with high potential applications in life sciences, personalized medicine, biotechnology, and ecological monitoring.[1−3] The fundamental approach of measuring ion currents passing through a protein nanopore in an insulator membrane, such as a lipid membrane or an artificial membrane made from an organic polymer, remains widely utilized and has undergone continuous development in recent years.[2,3] The analytes could be detected by a direct or indirect approach. In the direct approach, an applied potential across the membrane triggers the entry, trapping and potential translocation of the analyte through the pore. In the indirect approach, the pores capture or translocate the adaptor-analyte complex, only the analyte molecule, or the molecule that competes with the analyte for binding to the adaptor.[2] Each capture or translocation causes detectable specific current changes.[2,4] Such a nanopore approach has already been successfully applied for commercial ultralong DNA sequencing[5] and has notable potential for proteomic applications.[2,3,6−8] Nevertheless, there are three main challenges that prevent the promising nanopore-based protein fingerprinting or sequencing approach from following commercially available DNA sequencing. First, distinguishing between 20 proteinogenic amino acids that are susceptible to various post-translational modifications (PTMs) is more difficult compared to the four basic core DNA bases. Secondly, peptides and proteins fold in a three-dimensional (3D) structure, which could make the capture and translocation of molecules less straightforward. In addition, unevenly distributed charges along the polypeptide chain may cause more complex interactions between the analyte and the pore, resulting in less controllable movement of the protein. All this leads to complex nanopore signals, which may be more challenging to process and understand. To overcome these challenges, direct and indirect approaches have been explored to detect folded proteins with different molecular weights,[9,10] to track protein unfolding kinetics,[11] binding affinities,[12] and various PTMs such as ubiquitination,[13,14] phosphorylation,[15−17] acetylation,[18] propionylation,[19] and glycosylation,[16] as well as to detect sequence variations[20,21] and amino acid chirality.[22,23]

Proteins play a key role in most biological processes and changes of their concentration in biological samples often correlate with diverse pathological conditions, making them suitable biomarkers alongside nucleic acids and small organic molecules.[24] Through intensive proteomic analyses in recent years, histones have gained attention as potential biomarker molecules.

Received: September 23, 2025
Revised: January 28, 2026
Accepted: February 3, 2026
Published: February 20, 2026

https://doi.org/10.1021/acssensors.5c03533
ACS Sens. 2026, 11, 2016−2029

In addition to their physiological canonical function in DNA packaging and regulation of gene expression in the cell nucleus, histones also have extracellular functions. They have antimicrobial functions and can act as damage-associated molecular patterns (DAMPs)[25−28] and are a predominant protein in neutrophil extracellular traps (NETs).[26,29] Their elevated serum levels correspond, for example, to disease activity in patients with rheumatoid arthritis (RA),[30] cancer prognosis,[31] cardiac arrest,[32] urosepsis,[33] and trauma.[28] In contrast to established protein detection techniques such as mass spectrometry and immunoassays, particularly in the case of histones, nanopores could offer rapid, real-time, high-throughput detection of single molecules, especially when integrated into small portable devices.[5]

The most important prerequisite for optimal molecule detection is the compatibility of the pore diameter and size of the analyte.[19,34,35] Due to the large variety of proteins compared to nucleic acids, novel pores with the desired properties are in high demand. Actinoporins, pore-forming toxins present in venom of sea anemones,[36] form pores by bundle of α-helices.[37−40] Pore formed by fragaceatoxin C (FraC), from sea anemone *Actinia fragacea*, was shown to be composed of eight identical protomers[40] and was employed for nanopore sensing applications to discriminate nucleic acids,[41] detect PTMs in selected proteins,[16] and discriminate peptides of different lengths.[42] FraC pores have not yet been used for the detection of full-length folded proteins. In the present work, we implemented a novel octameric actinoporin pore[43] for the detection and identification of medically relevant histone variants. We prepared a pore construct that stably inserts into polymeric MinION membranes, implemented in commercially available DNA sequencing devices. This allowed us to detect different human histones as well as quantify mixtures of two medically important extracellular histones using a machine learning approach.

■ RESULTS AND DISCUSSION

Wild-Type Fav Pore Optimization for Stable Insertion into Lipid and Polymeric Membranes

We have recently described a novel, conically shaped pore formed by an actinoporin-like homologue from the coral *Orbicella faveolata* (wild-type Fav, wtFav) (Supporting Information Figure S1).[43] Compared to FraC pores,[40] wtFav pores are similarly organized. The pore consists of two distinct regions. The cap on the *cis* side of the membrane is formed by circularly arranged β-sandwiches of protomers. Each of these protomers also contributes a single α-helix to form the transmembrane region (Figure 1a). wtFav has an additional, 82 amino acid long, unstructured N-terminus extending on the *trans* side of the lipid bilayer (Figure 1a, Supporting Information Figure S1). We attempted to incorporate wtFav pores into polymeric MinION membranes, but they could not be readily incorporated (Supporting Information Figure S2). Efficient insertion was likely limited by the long unstructured N-terminus, which has been shown to inhibit the permeabilization activity of other actinoporins.[37,39]

To address this issue, we made a series of constructs with different deletions of the N-terminus (Supporting Information Figures S1 and S2). All isolated constructs formed oligomers on large unilamellar vesicles composed of 1,2-dioleoyl-*sn*-glycero-3-phosphocholine (DOPC):sphingomyelin (SM) (1:1, mol:mol), and detergent-extracted pores could be inserted into polymeric MinION membranes (Supporting Information Figure S2). The most promising variant, based on insertion efficiency into polymeric MinION membranes, was ΔN67Fav (Figure 1a,b, Supporting Information Figure S2), missing 67 N-terminal residues. The shortest construct tested, ΔN75Fav, which corresponds to the length of FraC (Supporting Information Figure S1), showed unstable current and compared to other constructs, it exhibited a lower current signal with considerable noise, especially at applied negative voltages below −100 mV (Supporting Information Figure S2b). We also observed an increased loss of pore signal after repeated measurements on the same flow cell (which was rarely observed with other constructs), presumably due to weaker insertion into the polymeric membrane. However, all tested constructs showed a broad distribution of open pore current at −90 mV (Supporting Information Figure S2c), which prevented us from performing experiments with single pores.

To improve the insertion of pores, the distribution of open pore currents and baseline signal-to-noise ratio (defined as the mean open pore current divided by its standard deviation) of Fav nanopores, we used the 3D structure of the wtFav pore to introduce point mutations using site-directed mutagenesis[44,45] (Figure 1a). Briefly, nine positions occupied by glutamate or aspartate residues were identified as non-conserved in over 100 Fav homologues. Each of these positions was then, in shortest tested construct ΔN75Fav, mutated to amino acids that naturally occupy these positions in Fav homologues, resulting in 20 single amino acid mutants. Each of these mutants was tested for hemolytic activity. Those that showed similar or better activity than the wtFav were further selected to generate nine double amino acid mutants. Of these mutants, one (termed RN-Fav) showed stable and discrete insertion into lipid bilayers at negative voltages and a significantly improved baseline signal-to-noise ratio. RN-Fav corresponds to the approximate size of FraC, beginning with R77 (Figure 1, Supporting Information Figure S1a), and in addition carries two mutations of the charged, non-conserved amino acids D203R and D215N (Figure 1a). These mutations improved the pore stability in the membrane and distribution of the open pore current to a certain extent but not the baseline signal-to-noise ratio (see below). The RN1-Fav pore was, therefore, designed. Here, we used the best construct in the terms of insertion efficiency, ΔN67Fav, and included mutations D203R and D215N of RN-Fav. In addition, we replaced all positively charged residues in the unstructured N-terminus with negatively charged or polar ones (Figure 1a). This construct also contained four substitutions of amino acid residues with aromatic side chains in the transmembrane α-helical region with an attempt to reduce the fenestrations between the α-helixes in the transmembrane region (Figure 1e, Supporting Information Figure S1) where lipid binding has been observed and may represents a potential entry point for ions or small molecules.[43]

Compared to FraC, which mostly forms octameric pores[40] and, under certain conditions, heptameric and hexameric pores (whose structures have not yet been determined),[42] wtFav oligomerizes into octameric and some nonameric pores (Figure 1b), the latter of which are not stable when solubilized if the lipid membrane used for oligomerization does not contain cholesterol.[43] RN-Fav and RN1-Fav variants showed an altered octamer:nonamer ratio compared to ΔN67Fav (Figure 1b, Supporting Information Figures S3 and S4). Due to the different net charge, resulting from the difference in stoichiometry

https://doi.org/10.1021/acssensors.5c03533
ACS Sens. 2026, 11, 2016−2029

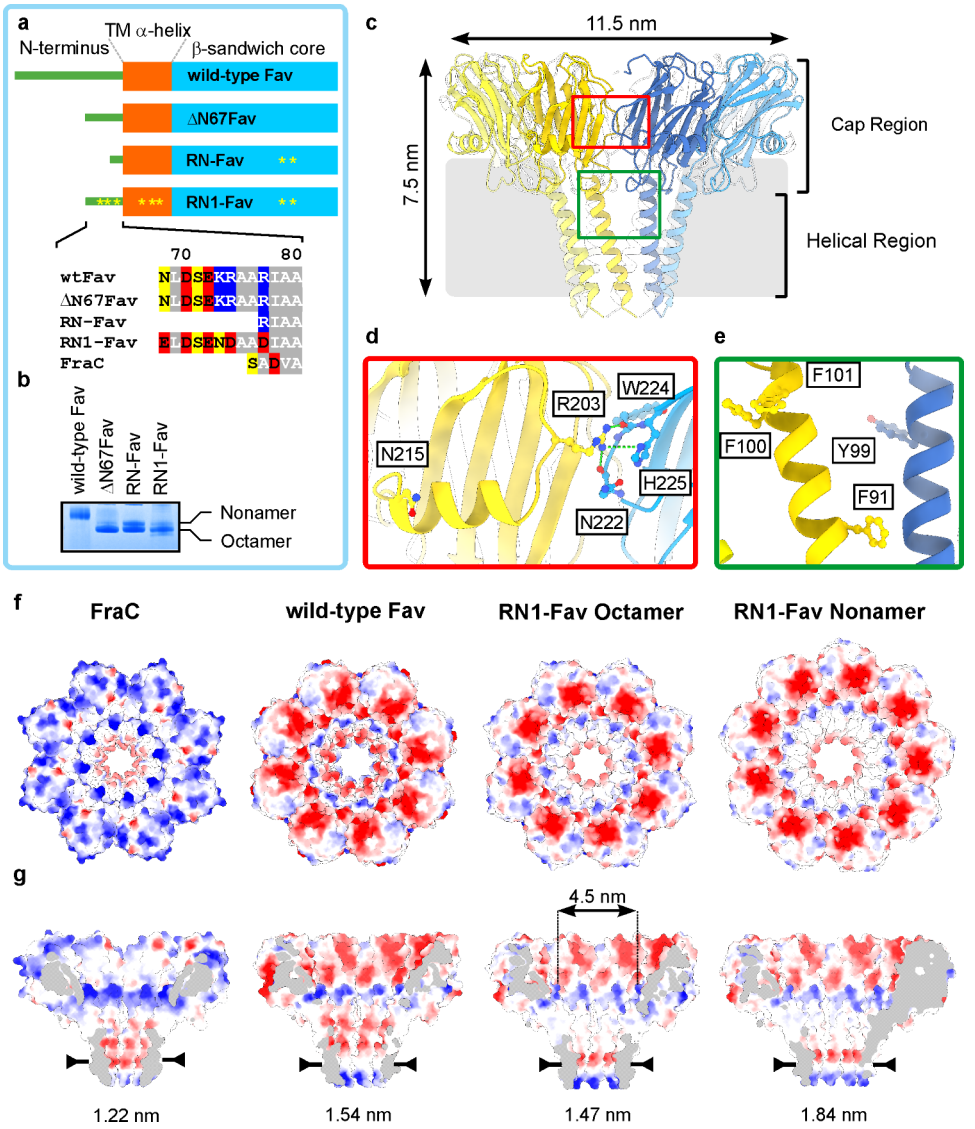

Figure 1. Structural characterization of RN1-Fav pores. (a) A schematic representation of the proteins used in this study. The positions of the mutations are indicated by yellow stars. The sequences of the N-termini of different constructs used in this study are shown enlarged. wtFav, wild-type Fav. Yellow, polar residues; red, negatively charged residues; blue, positively charged residues, gray, hydrophobic residues. Fragaceatoxin C (FraC) is shown for comparison. The numbering is according to the wtFav. N-terminal 67 residues of the wtFav are not shown. See the alignment in Supporting Information Figure S1 for details. (b) Native PAGE gel of the pores used in this study. The position of octamers and nonamers is indicated. (c) Overall architecture of the octameric RN1-Fav pore model solved by cryo-electron microscopy. Black arrows indicate the overall dimensions of the pore. The putative membrane region is shown as a gray rectangle. Red and green rectangles are shown enlarged in panels (d) and (e). (d) The magnification of the pore structure around residue R203, which shows formation of H-bonds with neighboring side chains of the other protomer. Side chains of the indicated amino acid residues are shown in ball and stick presentation. Blue balls, nitrogen; red balls, oxygen; green dotted line, potential H-bonds. (e) The magnification of the helix region with all mutated residues in RN1-Fav presented in ball and stick presentation. (f, g) Electrostatic potential of the FraC (PDBid: 4TSY), wtFav (PDBid: 9EYM), and RN1-Fav pores (PDBids: octamer: 9EYP, nonamer: 9EYQ), top view (f) and cross sections (g), with the color gradient from negative (red) to positive (blue) potential. The pore constriction is highlighted with arrows, and the diameter is indicated. The dimensions of the pore lumen in the cap region are also indicated for the octamer of RN1-Fav.

of protomers, homogeneous preparations of octameric or nonameric pores could be obtained by ion-exchange chromatography (Supporting Information Figure S5). Cryo-electron microscopy reconstruction of octameric and nonameric RN1-Fav pores at 3.05 and 3.3 Å resolution, respectively (Figure 1c, Supporting Information Figures S3 and S4, Supplementary Table S1), revealed that the introduced D203R mutation enables the formation of additional stabilizing H-bonds between adjacent protomers in the cap region on the outer side of the pore. Two H-bonds are formed, the first between the side chain of R203 of one protomer and the main chain carbonyl group of N222 or the side chain of H225 of the other protomer. The second is formed by the side chain of R203 and the main chain carbonyl group of W224 (Figure 1c,d). In contrast, the side chain of aspartic acid at the same position in wtFav is too short to allow the formation of these H-bonds. These additional contacts on the outer side of the pore help stabilize nonameric pores once solubilized, similar to how the presence of

https://doi.org/10.1021/acssensors.5c03533
ACS Sens. 2026, 11, 2016−2029

cholesterol and more tightly packed lipids stabilize nonamers in the case of wtFav.[43]

The side chains of the introduced aromatic residues in the helical region are oriented away from the lumen of the pore, except for Y99, which points toward the central pore axis (Figure 1c,e). When comparing the surfaces of the two fenestrations (upper and lower), the lower one, due to the introduction of phenylalanine at position 91, decreased by roughly 60% (Supporting Information Figure S4g). Larger hydrophobic side chains of F100 and F101 interact with lipids L1 and L6 and slightly change the position of L6 compared to its position in wtFav (Supporting Information Figure S4h). These additional interactions with lipids may stabilize the helical region of the pore and, therefore, reduce the noise (see below).

The RN1-Fav pores also differ in the diameter of the pore constriction compared to the FraC (diameter of 1.22 nm) and wtFav pores (diameter of 1.54 nm), with diameters of 1.47 and 1.84 nm for octameric and nonameric pores, respectively (Figure 1e, Supporting Information Figure S3). Due to the introduced mutations in RN1-Fav, the inner surface of the pore is less negatively charged than in wtFav, but still much more negative than in the FraC pore (Figure 1f,g).

RN-Fav and RN1-Fav Pores Have Improved Characteristics in Comparison to ΔN67Fav Pores

Although most common single-channel recording devices provide an excellent basis for the electrophysical characterization of pores,[42,46−48] they rarely achieve the desired high-throughput that can be achieved with devices such as the MinION. Variants of Fav pores incorporated stably into MinION membranes (Supporting Information Figure S2a), which enabled a desired high-throughput characterization. We characterized the RN-Fav and RN1-Fav pores in MinION flow cells and compared them with the ΔN67Fav pores, while wtFav did not insert into membranes. In all experiments, we used MinION flow cells and inserted the pores from the *cis* side of the membrane by employing a stepwise increasing voltage ramp from +30 to +300 mV. For the basic characterization of the pores, we used a voltage ramp with alternating voltage polarities from 0 to ±120 mV (in 10 mV steps). Membranes with a single inserted pore were selected based on the constructed histogram of open pore current at −50 mV, which included all active pores on the MinION flow cell.

The ΔN67Fav pore sample contains mostly octameric pores, because nonamers were not stable enough to withstand pore preparation steps and were not detected by cryo-electron microscopy analysis. It showed a broad distribution without recognizable, well-resolved peaks (Figure 2a−c). In addition, the I/V curve was highly asymmetric and showed high and noisy currents at negative potential, but the pore was almost closed at positive applied potential (Figure 2c). In contrast, the changes introduced in the RN-Fav and RN1-Fav pores resulted in narrower current distributions (Figure 2b), altered the shape of the I/V curves, increased the current at positive applied potential (Figure 2c), and significantly increased the baseline signal-to-noise ratio at −50 mV (Figure 2d). In addition, both the nonameric RN-Fav and RN1-Fav pores showed a higher open pore current compared to the octameric pores due to the larger pore diameters (Figure 1e). In all histograms ∼20% variability of the open pore current is observed. While they represent data from one flow cell, this is most likely due to pore-to-pore and could originate from the more dynamic transmembrane part of the pore compared to β-barrel pores (Supporting Information Figure S6b−d).

The linearization of the I/V curve can be attributed to changes at the N-terminus of RN-Fav and RN1-Fav (Figure 1a). The long and unstructured positively charged N-terminus of ΔN67Fav could clog the pore when a positive voltage is applied (Figure 2b). Removal of a significant portion of the N-terminus in RN-Fav, which could not clog the pore, and additional mutations in RN1-Fav, which reduced the repulsion between the previously positively charged N-terminus and the positively applied voltage at the grounded electrode on the *trans* side of the membrane, resulted in more linear I/V curves and open pores at the positively applied voltages (Figure 2c). The effect was more pronounced for RN1-Fav pores compared to RN-Fav pores (Figure 2c).

The RN1-Fav pores exhibited a significantly better baseline signal-to-noise ratio compared to ΔN67Fav and RN-Fav pores (Figure 2d), which was determined as the open pore current value at −50 mV (I_0) divided by the standard deviation of the open pore current at −50 mV. The substitution of positively charged amino acids in RN1-Fav affected the protonation of the pore lumen (Figure 1f,g). The effect of charge distribution alongside the pore lumen on the baseline signal-to-noise ratio was already reported for OmpF[49] and MspA.[50] At −50 mV, the RN1-Fav pore remained open throughout the experiment and did not show any spontaneous gating (Supporting Information Figure S6a). The noise of the RN1-Fav pores is, however, higher in comparison to β-barrel pores, such as lysenin[51] (Supporting Information Figure S6b−d). This is most likely due to the more flexible transmembrane region, which in RN1-Fav is represented by a bundle of α-helices and is, according to molecular dynamics simulation, more flexible than the β-barrel of the lysenin pore (Supporting Information Figure S6e,f). Overall, the improved open pore current distribution together with the increased open pore current at negative voltage, significantly increased baseline signal-to-noise ratio, and, on average, 325 pores (calculated from 5 MinION flow cells), representing 96.7% of all single pores detected (40% of all MinION membranes with pore signal), made the octameric RN1-Fav pore (Figure 2d,e) a promising candidate for high-throughput protein detection and identification purposes.

Histone Trapping in RN1-Fav Pores

Since the RN1-Fav pores stably insert into the MinION membranes and showed improved electrophysical properties compared to the ΔN67Fav and RN-Fav pores, we tested the octameric RN1-Fav pores for detection and identification of human histone variants. We chose octameric pores because we achieved a higher number of single inserted pores compared to nonameric pores (Figure 2b) and the fraction of octameric pores after ion-exchange chromatography was more homogeneous (Supporting Information Figure S5). The charge of the pore vestibule is considered one of the most important parameters for electrostatic interaction between analytes and the pore.[52,53] We hypothesized that negatively charged RN1-Fav pores (Figure 1f,g) would be able to discriminate positively charged human histone variants (Figure 3a) depending on their net charge. Histones are approximately 15 kDa molecules with an ordered globular domain and an unstructured N-terminal tail (Figure 3a−c) when in the bound state in nucleosomes and less structured in the absence of a binding partner. According to AlphaFold predictions, α-helical secondary structures are still

https://doi.org/10.1021/acssensors.5c03533
ACS Sens. 2026, 11, 2016−2029

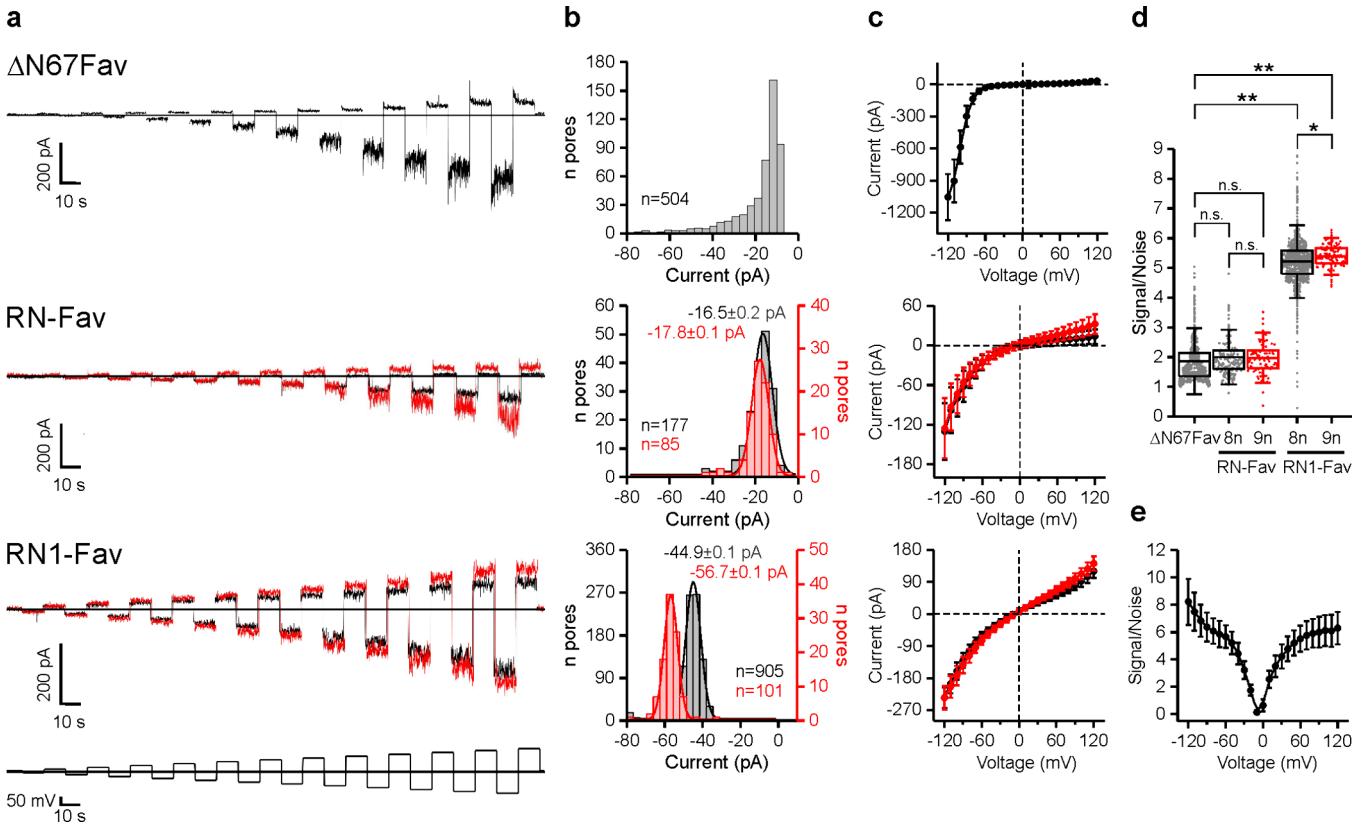

Figure 2. High-throughput electrophysical characterization of Fav pores. (a) Representative current traces recorded with the MinION system after applying a 10 mV step voltage ramp from 0 to ± 120 mV. The black straight line marks 0 pA or 0 mV. Black, data for the octameric pore; red, data for the nonameric pore. (b) Current histogram of the open pore at −50 mV with Gaussian fits where applicable. The number of pores (n), included in analysis also in panels (c−e), is given for each variant. We also report the mean current ± standard deviation for all RN-Fav and RN1-Fav pores resulting from the fits. (c) An averaged I/V curve for all detected single pores per MinION flow cell recorded with the same ramping protocol as in (a), with the corresponding standard deviations. (d) Box plot showing the baseline signal-to-noise ratio at −50 mV, calculated for all single pores. Center line, mean; box limits, upper and lower quartiles; whiskers, SD; all data points are shown. The difference was tested with the two sample t-test. $^{**}p < 0.01$, $^{*}p < 0.05$, n.s. stands for no statistical difference ($p > 0.05$). (e) Mean baseline signal-to-noise ratio ± standard deviation for RN1-Fav octameric pores over the entire voltage ramp, calculated for the pores included in other panels. All traces were recorded at 20 kHz sampling rate and filtered with a 5 kHz low-pass filter.

present in solution and N-terminal tails are structurally disordered (Figure 3c). The N-terminal tails are susceptible to PTMs (Figure 3b).[54] Histone H4 (net charge: +17.3, N-terminal tail net charge +7.3) has a 24 amino acid N-terminal tail and core domain of 79 amino acids (Figure 3c). Histone H3.1 (net charge: +19.4, tail net charge +12.6) is slightly larger and has 39 amino acids long N-terminal tail and 97 amino acids core domain (Figure 3c).

Since histones are known to be highly post-translationally modified, we also characterized histones H3K9ac (net charge: +18.4, tail net charge +11.6) and H3K23ac (net charge: +18.4, tail net charge +11.6) with a single acetylated lysine residue at positions 9 and 23, respectively, and H3Cit (net charge: +10.4, tail net charge +7.6) with all together nine citrullinated arginine residues (Figure 3b). The dimensions of the histone core domain, when compactly folded in nucleosomes, are approximately 5.9 × 3.8 × 2.5 nm for H3.1 and 5.9 × 2.9 × 2.3 nm for smaller H4 (estimated with ChimeraX[55]). Since the width of the RN1-Fav octameric pore lumen is approximately 4.5 nm (Figure 1g), these dimensions would allow the histones to be captured into the pore from the *cis* side.

All experiments with histones were performed at negative voltages, as the histones are positively charged and the electrophoretic force would therefore help to trap them in the negatively charged lumen of the pore.[56] The capture of histones already started at voltages below −30 mV. In the case of H4, the smallest histone based on molecular weight, most pores showed well-resolved discrete blockades at −40 and −50 mV, but at higher voltages, the blockades became longer and only changing the voltage polarity restored the open pore current, except in cases where pores were destabilized and fall out of membrane (Supporting Information Figure S7). Interestingly, after applying −90 or −100 mV to pores that stayed open (82% and 45% of all pores, respectively), only a few discrete blockades occurred, and intense current fluctuations prevented us from accurately determining the blockades (Supporting Information Figure S7). Similar blockades, but with long-lasting pore occupancies even at lower voltages, were observed for larger and more positively charged H3.1. Furthermore, at voltages below −80 mV, membranes with inserted pores rarely remained intact (Supporting Information Figure S8). The observed long-lasting pore occupancies accounted for less than

https://doi.org/10.1021/acssensors.5c03533
ACS Sens. 2026, 11, 2016−2029

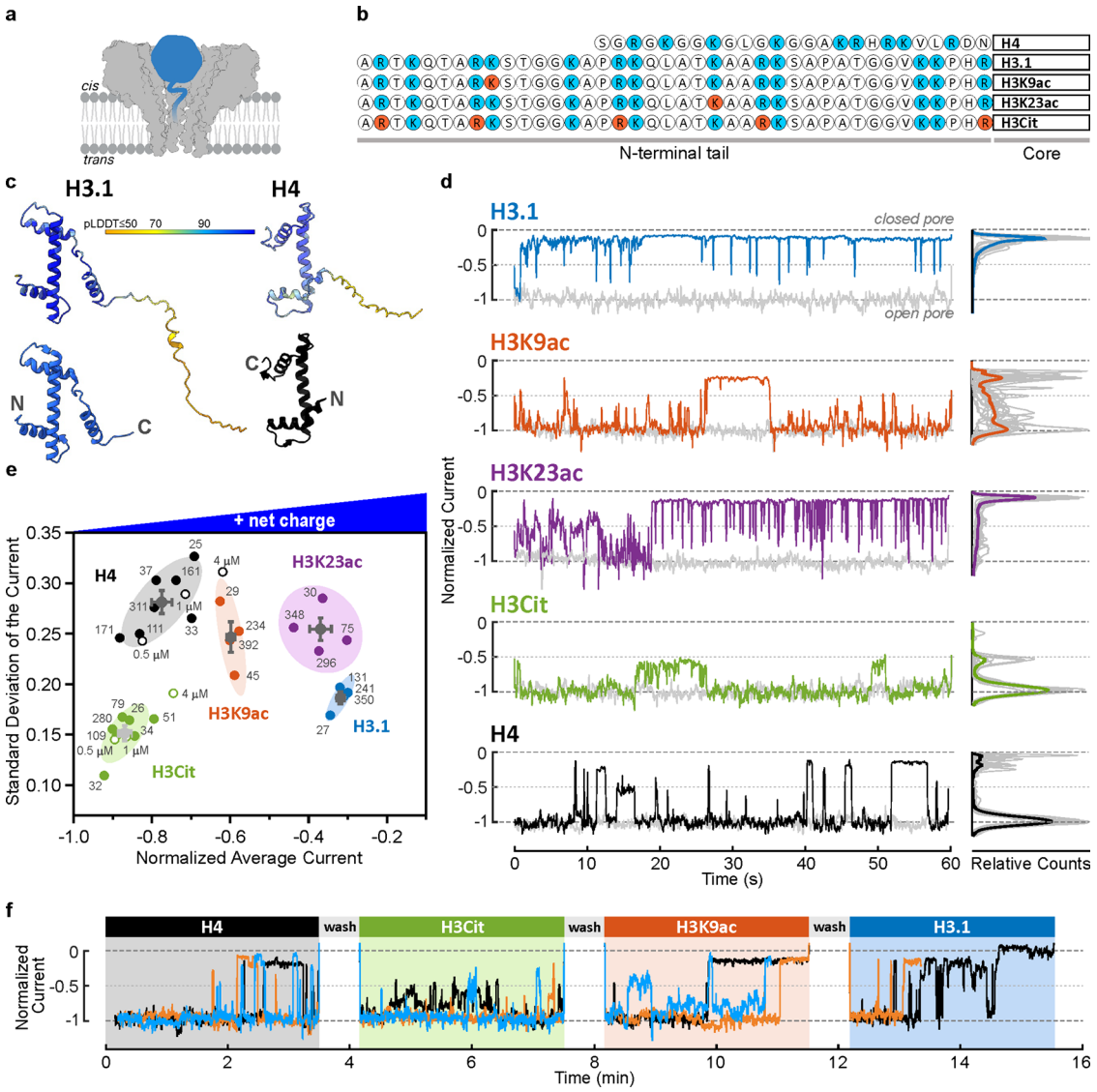

Figure 3. Label-free differentiation of human histone protein variants by bulk analysis. (a) A schematic model of full-length histone detection (blue) with an octameric RN1-Fav pore. The histones were added from the *cis* side of the membrane. (b) Amino acid sequences of the unstructured N-terminal histone tails of the histones used in this study. Amino acids with positively charged side chains are colored blue and post-translationally modified amino acids are colored red. (c) The top row shows structures predicted by AlphaFold for histones H4 and H3.1 (colored according to per-residue confidence score (pLDDT); parts with higher model confidence are colored blue and those with the lowest model confidence are colored orange). The bottom row shows 3D models of histones H3.1 (blue) and H4 (black) core domains (PDBid: 2CV5)[57] with N- and C-termini labelled. (d) Representative normalized one-minute current traces recorded at −50 mV. The gray traces represent control measurements of the same pore in the absence of histones, while the colored traces correspond to current traces obtained after the addition of 2 μM histone as indicated. Gray curves on the right side are relative frequency histograms of 21 current traces (the one on the left side and 20 from Supporting Information Figures S11−S15), while colored bold lines are their mean values. (e) Discrimination of histone variants based on normalized average current and standard deviation of the current for the 60 s long current traces of individual pores recorded simultaneously with a single flow cell (each circle represents a MinION flow cell and the corresponding number of individual pores included in the analysis is stated in gray color). The standard error of the normalized average current and standard deviation of the current are shown as gray error bars. Additionally, mean values for 0.5, 1, and 4 μM histones H4 and H3Cit are plotted as open circles with concentrations indicated. Each point represents an average from three independent flow cells, the number of individual pores at each flow cell was from 22 to 303. (f) Three normalized current traces from the same flow cell (black, orange, and blue) recorded at −50 mV during sequential addition of histones H4 (1 μM), H3Cit (4 μM), H3K9ac (2 μM), and H3.1 (2 μM) with intermediate buffer washing steps at 50 mV. All traces were recorded at 20 kHz sampling rate and filtered with a wavelet filter.

8% of all blockades. As the absolute voltage increased, the dwell time of long-lasting blockades increased in the presence of histone H3.1 and decreased in the presence of histone H4. The average amplitude of long-lasting blockades was higher compared to short discrete blockades. Thus, the most likely explanation is that we observe histone trapping at lower voltages, while higher voltages could possibly trigger histone translocation with concurrent destabilization of the transmembrane

https://doi.org/10.1021/acssensors.5c03533
ACS Sens. 2026, 11, 2016−2029

α-helical bundle of RN1-Fav leading to intense current fluctuations (Supporting Information Figures S7 and S8).

For comparison, we prepared FraC pores and inserted them in MinION membranes. The insertion was less efficient than for the RN1-Fav, the pore did not remain stably inserted and there were no current blockades observed in the presence of H4 (Supporting Information Figure S9). These results additionally indicate that interactions of histones with RN1-Fav are possible due to its unique structural properties and net charge compatibility. For further experiments we chose −50 mV applied voltage for recording histone capture, as we could observe distinction of blockades at −50 mV and the baseline signal-to-noise ratio increases dramatically up to −50 mV and does not improve significantly at higher negative voltages (Figure 2e).

RN1-Fav Pores Enable Identification of Human Histone Variants

In the presence of 2 μM histone variants at an applied voltage of −50 mV, changes of the open pore current occurred in all histone samples, however, with different patterns (Figure 3d). After the addition of histone H3.1, short-lived mostly indiscreet changes occurred at the beginning of the one-minute trace, and soon thereafter, the current reduced almost completely, with some short-lived pore openings observed (Figure 3d). Similar traces were observed for the acetylated histone variant H3K23ac, but with more frequent short-lived pore openings, that most probably originate from disruption of pore and histone electrostatic interaction, while they disappeared in the presence of histone H3K9ac and H3Cit. In both cases, the open pore current recovered after applying voltages of opposite polarity (Supporting Information Figure S10), further confirming that histones were trapped in the pore and ejected from the pore when the voltage polarity was reversed. The presence of 2 μM histone H3K9ac resulted in higher current noise but also showed discrete current changes and rare long-lasting ones. Similarly, the addition of histone H3Cit and H4 resulted in discrete changes, with clearly qualitatively different current traces, excluding the possibility that observed patterns originate from pore-to-pore variability (Figure 3d, Supporting Information Figures S11−S15, Supplementary Table S2).

First, we investigated whether we could distinguish histones based solely on the average mean current of single pores in the presence of the analyte, i.e., without blockade extraction and comparison. We calculated the normalized average current of individual pores in the presence of histones for the entire duration of the experiment (60 s, unless otherwise stated) and the standard deviation of the current (Figure 3e, see raw data traces in Supporting Information Figures S11−S15). The normalized average current in the presence of the histones roughly correlated with the net charge of the histones (Figure 3e). The addition of H3.1 with the highest positive charge resulted in the lowest average normalized current (−0.32 ± 0.01) and the pores were blocked for almost the entire measurement period (Figure 3d,e). Similar long-lasting changes were observed for H3K23ac with the higher average normalized current (−0.37 ± 0.03), but they occurred later compared to histone H3.1 (Figure 3d). Interestingly, acetylation at a position further away from the core region in H3K9ac reduced the long-lasting changes and resulted in an average normalized current of −0.60 ± 0.01. H3Cit with the lowest net positive charge resulted in the appearance of discrete changes with an average normalized current of −0.88 ± 0.02 and almost no long-lasting current changes (Figure 3d,e). The smaller H4 showed a similar relative high current of −0.80 ± 0.03.

The bulk analysis approach could serve as a basic screening method for detecting specific analytes, although the results may be influenced by the applied voltage, the presence of impurities trapped in the pore, and changes in the analyte concentration. For example, when assaying increasing concentrations of H4 and H3Cit, we observed a decrease in the normalized average current and an increase in the standard deviation of the current, however, at each histone concentration they could still be distinguishably resolved (Figure 3e).

Significant changes in the current patterns between H3.1 and its acetylated variants H3K9ac and H3K23ac (Figure 3d, Supporting Information Figures S11−S15, Supplementary Table S2) suggest that the trapping signals most probably originate from specific sequence interactions between disordered histone N-terminal tails and the pore inner surface. Specifically, reduction of the positive charge at histone N-terminal tails away from the histone core (in H3K9ac) resulted in more discrete changes and reduction of long-lasting pore closures. The latest was further confirmed with sequential addition of histone H4, H3Cit, H3K9ac, and H3.1 in the same measurement, where each histone interacted with the same pore differently (Figure 3f). Histones were efficiently washed away from the pore by washing the flow cell with buffer solution at reversed voltage polarity.

In summary, such real-time bulk analysis allowed fast discrimination of histone variants by a combined bulk analysis of relative normalized average current and standard deviation of the current (Figure 3e, Supplementary Table S2).

Current Blockade Analysis Differentiates Medically Relevant Histones

Although bulk analysis allowed us to distinguish between histones when testing a single histone variant at a time, we then performed a detailed blockade analysis, which allowed us to discriminate mixtures of histone variants. For each blockade, we determined the relative open pore current (I_0) at −50 mV and the mean blockade current (I_h), amplitude (determined as $(I_0 - I_h)/I_0$), the noise (standard deviation of the blockade current (I_h)), and the dwell time (Supporting Information Figure S16) were calculated for the blockades extracted by the threshold method. The blockades extracted from different MinION flow cells in the presence of a particular histone were grouped and further analyzed.

Due to the medical relevance and presence in serum samples[30,32,58] and their separation based on the results of the bulk analysis (Figure 3e), we focused on analyzing blockades caused by H4 or H3Cit (Figure 4a). H3Cit is larger (136 vs 103 amino acids) and less positively charged (net charge +11.4 vs +17.3) than H4. The highest blocking amplitude (0.83 ± 0.10) was observed for the shortest histone variant H4, while H3Cit caused blocking with smaller amplitudes (0.38 ± 0.08). Most likely, due to its smaller size, H4 could be trapped deeper into the pore lumen and thus hinder the current flow through the pore more than H3Cit, which is probably also exposed to a lower electrophoretic force due to its lower net positive charge. Differences were also observed in the blockade noise, which corresponds to blockade current fluctuations. Histone H4 caused blockades with the lower noise compared to histone H3Cit. Similarly, differences were observed when inspecting the blockade dwell times (Figure 4a). Here, H3Cit caused

https://doi.org/10.1021/acssensors.5c03533
ACS Sens. 2026, 11, 2016−2029

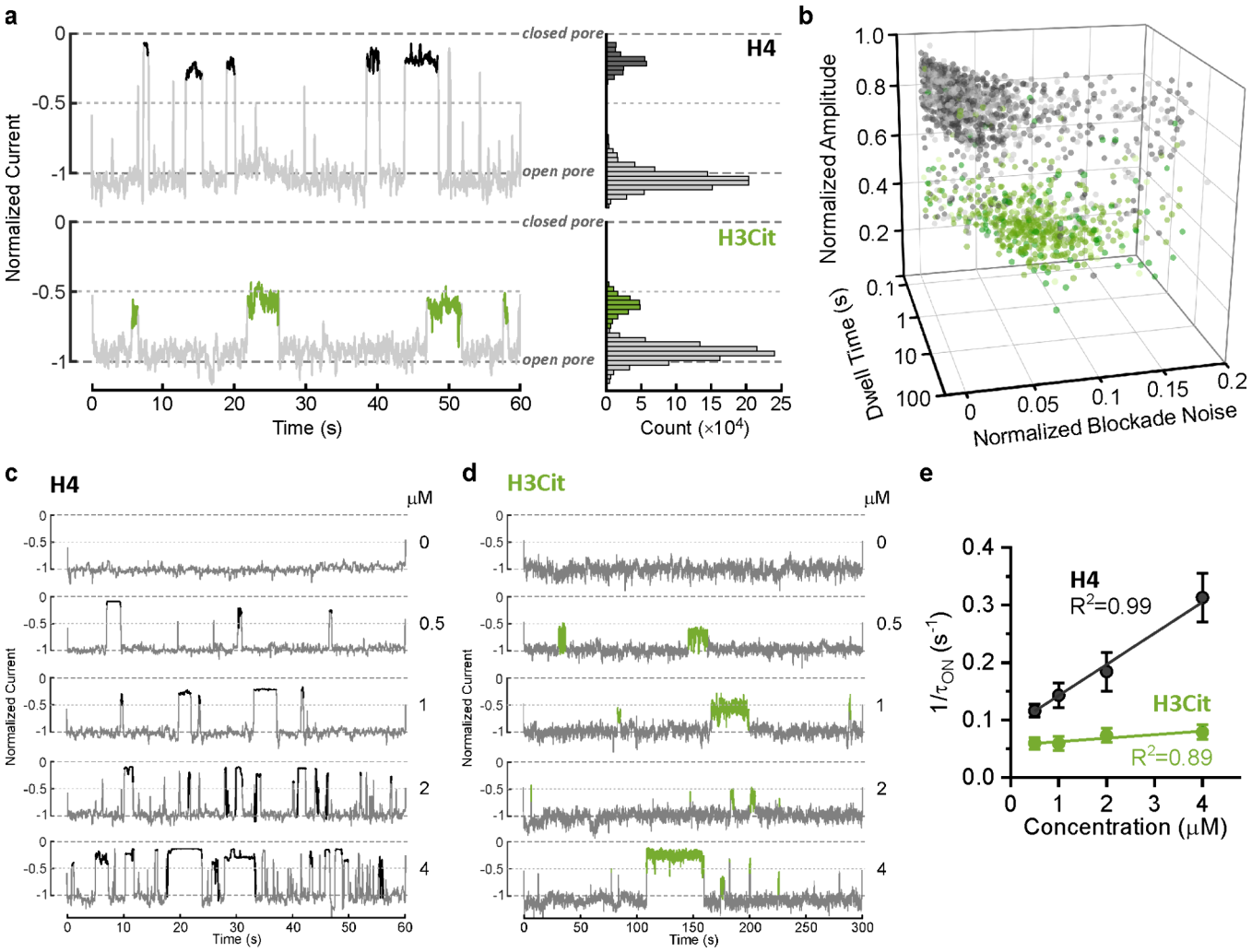

Figure 4. Histone discrimination based on blockade analysis. (a) 1 min current trace recorded at −50 mV in the presence of 2 μM histones. The colored sections of the trace represent the detected current blockades for H4 (black) and H3Cit (green). The histograms on the right side of each trace correspond to the current trace on the left side. The bars representing the detected blockade currents are shown in the corresponding colors. (b) 3D scatter plot of normalized blockade noise, amplitude, and dwell time for the blockades extracted from three independent flow cells in the presence of 2 μM histone (the data for each flow cell are shown as circles with different black (for H4) or green (H3Cit) intensities). For H4 data, 534, 260, and 460 blockades were extracted from flow cells with 179, 39, and 120 single pores, respectively. For H3Cit, 110, 386, and 42 blockades were extracted from 40, 280, and 25 pores, respectively. (c, d) 1 min current traces (low-pass filtered with a 1000 Hz cutoff) after addition of 0, 0.5, 1, 2, and 4 μM histone H4 (c) or 3 min current traces for histone H3Cit (d). (e) Linear fit to the concentration-dependent blockade frequency ($1/\tau_{ON}$). The data represent an average ± standard error calculated for 3−6 independent flow cells. All traces were recorded at a 20 kHz sampling rate and filtered with a wavelet filter.

longer blockades than H4 (Figure 4a). When plotted in 3D space based on the blockade's amplitude, noise, and dwell time (Figure 4b), we were able to clearly discriminate between these two important extracellular histone variants.

In addition, we tested whether RN1-Fav pores would also allow us to quantify histones based on their blockade frequency. In a series of experiments on the MinION flow cells with increasing concentrations of H4 (Figure 4c) or H3Cit (Figure 4d) (at a concentration of 0.5, 1, 2 or 4 μM), the observed blockade frequency for both histones, determined as $1/\tau_{ON}$ (time between the blockades), correlated linearly with histone concentration (Figure 4e). Importantly, even a short measurement, 3 min in the case of H3Cit, enabled quantification of the histones and thus showed great potential for rapid real-time detection of histones compared to the established, longer duration detection methods.

RN1-Fav Pores Allowed Discrimination of Medically Relevant Extracellular Histones in a Mixture

In a real biological sample, histones rarely occur in a single variant. Therefore, we tested whether RN1-Fav pores allow the discrimination of multiple histone variants in a mixture using machine learning. Machine learning has recently been adapted to analyze nanopore events[59,60] while providing fast and automatic predictions based on the raw data. At the same time, it avoids possible human bias, especially when working with more complex data sets. The input data used to train and test the model were the extracted blockades from the previously

https://doi.org/10.1021/acssensors.5c03533
ACS Sens. 2026, 11, 2016−2029

mentioned blockade current analysis collected from several independent flow cells (Figure 5a).

The model based on the k-nearest neighbor (kNN) algorithm resulted in a classification accuracy of 0.885 in the case of the histone H4, H3Cit, and H3K9ac mixture or 0.913 when analyzing a mixture of H3.1 and H4 (Supporting Information Figure S17) and 0.979 for the mixture of histones H4 and H3Cit (Figure 5a). The tested blockades were obtained using the same blockade extraction procedure as before and were extracted from the traces obtained after applying mixture of all three histones (Supporting Information Figure S17) or histones H4 and H3Cit in different molar ratios (1:0, 3:1, 1:1, 1:3, and 0:1) at a final histone concentration of 2 μM (Figure 5a,c). While the other two mixtures give promising results and demonstrate RN1-Fav pore sensitivity, we proceeded with detailed event prediction only for the more medically relevant H4/H3Cit mixture. The assessment of the predictive capacity of the obtained model was based on the number of blockades categorized as H4 or H3Cit blockade (Figure 5c,d) and showed a clear linear dependence (Figure 5e).

■ CONCLUSIONS

Hereby, we developed a RN1-Fav protein nanopore, which is based on the actinoporin homologue from *Orbicella faveolata*. We were able to prepare Fav pores of different stoichiometries and successfully incorporated them into polymer membranes of a MinION device (Figure 2, Supporting Information Figure S2). We used MinION devices to increase the throughput. Additionally, artificial membranes are increasingly used in nanopore sensing, are more robust to higher voltages, and are less affected by biological samples such as human serum.[62,63] We show data for several tens to several hundreds of individual pores (Figures 3e, 4, and 5, Supporting Information Figures S10−S15). This strategy allows obtaining data from many pores simultaneously to improve statistics and derive useful conclusions even in cases where pores are not superior in some features, such as noise as is the case for RN1-Fav pore (Supporting Information Figure S6).

The RN1-Fav pore complements the nanopore toolbox for sensing peptides and proteins. ClyA pore[64] is approximately two times wider than octameric RN1-Fav and can accommodate larger proteins.[65] Narrower pores such as aerolysin[15,18,20,66] or α-hemolysin[67] allow sensing of peptides[18,66] or extended polypeptide chains,[11,67] respectively. In addition, the RN1-Fav nanopore presented here enriches the existing range of conical protein nanopores, which were previously limited to FraC and more recently to YaxAB.[10] Compared to cylindrical nanopores, conical pores enable the capture of a wider range of protein analytes with greater mass. In addition, the distribution of negative charges in

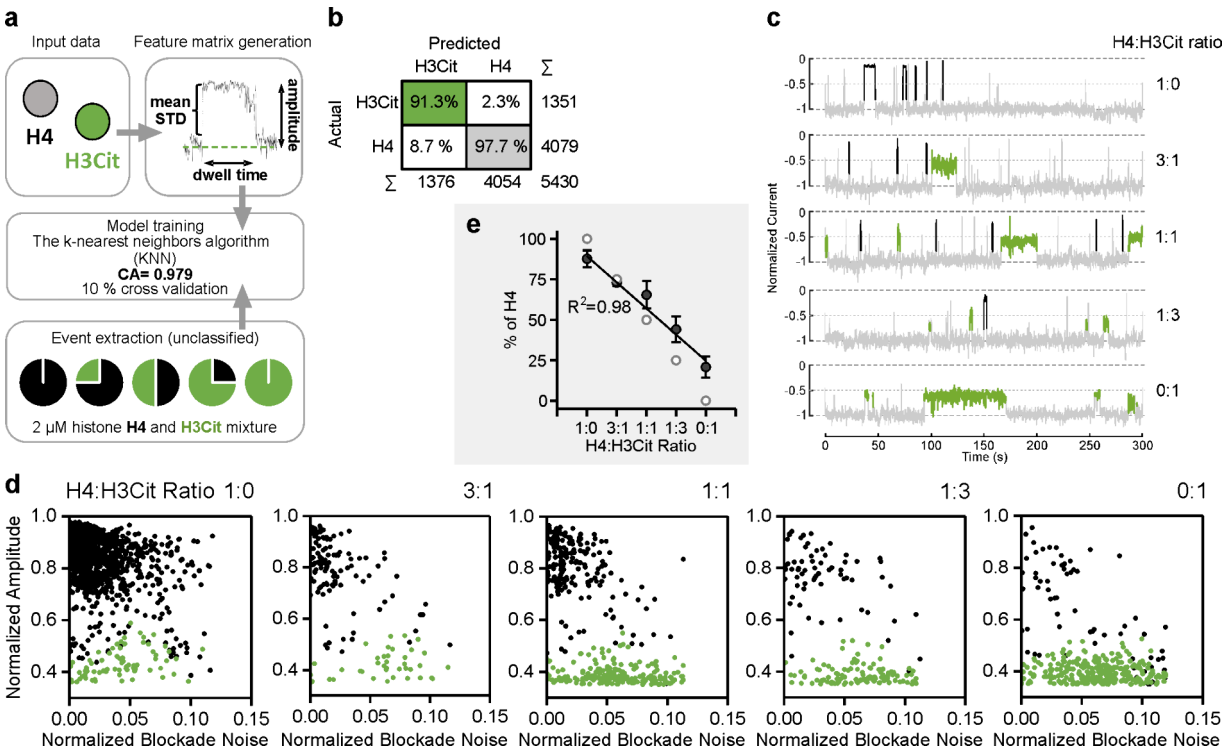

Figure 5. Machine learning supports the discrimination of histones in a mixture. (a) A workflow diagram of blockade classification by using Orange.[61] For training the model, the amplitude, blockade noise, and dwell time of the blockades extracted from the traces where only H4 or H3Cit was added were used as input data for future matrix generation. The model with a classification accuracy (CA) of 0.979 was generated using the kNN algorithm and cross-validating 10% of the data. (b) The confusion matrix generated with the data from the test set (random 20% of the input data) resulted in an accuracy of 91.3% for histone H3Cit and 97.7% for histone H4. (c) Blockades (bold parts of the traces) whose parameters were extracted from a 3 min trace where 1:0, 3:1; 1:1, 1:3, and 0:1 H4 and H3Cit ratios (at a total concentration of 2 μM) were used for classification based on the previously learnt model. The colors correspond to the blockades recognized as H3Cit (green) or H4 (black). (d) The experimentally determined ratio of histones in the mixture is based on the number of blockades classified as H4 (black) or H3Cit (green) out of a total of 1238, 158, 381, 176, and 347 input blockades. (e) Model-based estimation of the proportion of H4 in the mixture (black circles with linear fit) compared to the predicted theoretical values (open circles). The data represents an average ± standard error of three independent flow cells. All traces were recorded at a 20 kHz sampling rate and filtered with a wavelet filter.

https://doi.org/10.1021/acssensors.5c03533
ACS Sens. 2026, 11, 2016−2029

the lumen of the Fav nanopore differs from FraC, further diversifying the range of nanopore platforms available and allowing label-free capture and discrimination of positively charged analytes such as histones without prior unfolding.

Histones, in particular H4 and H3Cit, are becoming frequently proposed as potential biomarker molecules in serum.[28,30,68] Previously, nanopores were able to detect methylated and acetylated histone H4 peptides[18] or the whole nucleosome complex.[69] The RN1-Fav pore in combination with the MinION platform enabled us to detect full-length human histones without prior sample preparation. In particular, the required sample preparation steps for mass spectrometry and the required additional material for immunodetection are not needed.[70,71]

We distinguished between the full-length histone proteins H4 and H3.1 and their post-translationally modified variants. Furthermore, using machine learning, we were able to quantify and distinguish two biomedically important extracellular histones, H4 and H3Cit, in mixtures. Our results represent a new step toward the development of a fast, accurate single-molecule method for real-time monitoring of histone proteins in human body samples.

METHODS

Materials

All used chemicals, if not otherwise specified, were from Sigma-Aldrich (USA).

Strains and Protein Expression Constructs

The nucleotide sequences for Fav constructs were inserted into a modified pET28a (+) plasmid with the N-terminal 6 × histidine tag and TEV restriction site (ENLYFQGHM or ENLYFQS) and were used for transformation of *E. coli* DH5α. The following amino acids remain at the N-terminus of the mature proteins after cleavage with TEV:GHM in the wtFav and Δ67NFav or S in the case of RN-Fav and RN1-Fav (see the sequences of the mature proteins in Supporting Information Figure S1).

Expression and Purification of Recombinant Proteins

100 μL of competent cell *E. coli* BL21(DE3) strain was transformed with the plasmid, applied to agar plates with kanamycin resistance, and incubated overnight at 37 °C. A single colony was inoculated into 10 mL of the LB medium (supplemented with 30 μg/mL kanamycin) and incubated overnight at 37 °C and 180 rotations/min. The overnight culture was then added to 1 L of TB medium (30 μg/mL kanamycin, Gold Biotechnology (USA)) and incubated at 37 °C until reaching A_{600} = 0.8, when we induced protein expression with 0.25 mM isopropyl β-d -1-thiogalactopyranoside (IPTG, Gold Biotechnology (USA)). 16−18 h post-induction (incubated at 18 °C), we harvested cells by centrifuging the biomass at 4,000*g* for 10 min and at 4 °C. The cell pellet was washed with PBS (1.8 mM KH_2PO_4, 137 mM NaCl, 10 mM Na_2HPO_4, 2.7 mM KCl, pH 7.4), sonicated 2 × 7 min (1 s on, 2 s off), and centrifuged at 40,000*g* and 4 °C for 40 min. A soluble fraction was filtered through a 0.22 μm polyethersulfone filter and applied to the Ni-NTA column (Qiagen, Germany), washed with PBS, and eluted with PBS containing 0.5 M imidazole. Following overnight TEV digestion and dialysis against PBS, cleaved proteins were isolated by using another Ni-NTA chromatography step.

Large Unilamellar Vesicle Preparation

Multilamellar vesicles composed of sphingomyelin (from porcine brain; SM, Avanti Polar Lipids (Alabaster, AL, USA)) and 1,2-dioleoyl-*sn*-glycero-3-phosphocholine (DOPC, Avanti Polar Lipids (Alabaster, AL, USA)) in a 1:1 molar ratio at a 50 mM lipid concentration were prepared by dissolving lipids in chloroform (analytical standard, Sigma-Aldrich, USA). After removing solvent by using a rotavapor and formation of a thin lipid film, we resuspend the film in PBS by vortexing followed by six freeze and thaw cycles. LUVs of 100 nm in diameter were prepared by a single-use NanoSizer Extruder (T&T Scientific, South Korea).

Pore Isolation

150 μL of LUVs at 50 mM lipid concentration were mixed with soluble monomeric protein in a molar ratio 1:300 (protein:lipid) and incubated at 37 °C for 30 min. Vesicles were disrupted by adding lauryldimethylamine oxide (LDAO) to a final 0.75%, diluted in 50 mL of 50 mM Tris/HCl, 0.02% Brij 35, pH 8, and further purified by ion-exchange chromatography using 50 mM Tris/HCl, 2 M NaCl, 0.02% Brij 35 (Resource Q, Cytiva, USA) as an elution buffer, employed in a linear salt gradient. Pores eluted at approx. 0.3−0.5 M NaCl.

FraC pores were prepared in the same way as described above, except that the vesicles were solubilized by addition of *n*-dodecyl-β-d-maltoside (DDM) to 1% final concentration and diluted in 20 mM Tris/HCl, 0.02% DDM, pH 8, and further purified by ion-exchange chromatography using 20 mM Tris/HCl, 2 M NaCl, 0.02% DDM (Resource S, Cytiva, USA) as the elution buffer in a linear salt gradient.

Native PAGE

17 μL of pore sample (after ion-exchange chromatography) was mixed with 6 μL of native PAGE loading buffer (50 mM Bis/Tris, 6N HCl, 50 mM NaCl, 10% w/v Glycerol, 0.001% Ponceau S, pH 7.2) and G-250 (final concentration of 0.02%), centrifuged for 10 min at 16,000*g*, and loaded on 4-16% Bis/Tris gels. The running buffer was composed of 0.05 M Bis/Tris, 0.05 M tricine, pH 6.9, and the cathode buffer was prepared by mixing 190 mL of the running buffer with 10 mL of 20 × NativePAGE Cathode Buffer (Invitrogen, USA). After fixation in 40% methanol and 10% acetic acid solution, gels were washed in 8% acetic acid solution.

Cryo-EM Sample Preparation and Data Acquisition

3 μL of pore samples with concentration ∼1 mg/mL was applied to a glow-discharged (GloQube Plus, Quorum, UK) Quantifoil R1.2/1.3 mesh 200 copper holey carbon grid (Quantifoil, Germany), blotted under 100% humidity at 4 °C for 6−8 s, and plunged into the liquid ethane with a Mark IV Vitrobot (Thermo Fisher Scientific, USA). Micrographs of the RN1-Fav pore were recorded on a Glacios (Thermo Fisher Scientific, USA) with a Falcon 3EC direct electron detector (Thermo Fisher Scientific, USA) operated at 200 kV using the EPU software (Thermo Fisher Scientific, USA) at a nominal magnification of 190,000× and pixel size of 0.745 Å.

Cryo-EM Data Processing

All steps of data processing for all samples were performed in cryoSPARC v4[72] with built-in algorithms; the workflow is summarized in Supporting Information Figure S3a. Movies were aligned and dose-weighted with patch motion correction, and contrast transfer function (CTF) was estimated with patch CTF. Micrographs with an estimated CTF fit above 6 Å were excluded from further analysis. Initially, particles were picked by hand to generate 2D templates for template picking. Particles were extracted and underwent two rounds of 2D classification. Particles from the best 2D classes were used in *ab initio* reconstruction to generate 4 volumes. Among these 4 volumes, one corresponded to octameric and one to nonameric pore. Octameric and nonameric particles were separated and cleaned up by four iterations of two parallel heterogeneous refinements with 4 volumes each. In each round, one volume corresponded to the pore of target stoichiometry, octameric or nonameric. In addition, to the target volume, three decoy volumes were used. One of the decoy volumes was a volume of the other stoichiometry, e.g., if the octameric pore was a target,

https://doi.org/10.1021/acssensors.5c03533
ACS Sens. 2026, 11, 2016−2029

one of the decoy volumes was the nonameric pore, and *vice versa*, while the other two were random volumes generated during *ab initio* reconstruction. After each round, particles classified into the two junk decoy volumes were discarded and particles classified to the alternative stoichiometry were moved to the next step of the parallel refinement. For example, after the first round of heterogeneous refinement, particles that were classified to the volume of the nonameric pore where the target volume was octameric were combined with particles that classified to the nonameric volume in the process where the target was also nonameric, and *vice versa*. These two new particle stacks of octameric and nonameric pores were then used in the next round of heterogeneous refinement. After heterologous refinement, particles from the best 3D class were re-extracted using local motion correction and used in homogeneous refinement and subsequent non-uniform (NU) refinement with applied C8 or C9 symmetry.

Model Building

Atomic models of protomers were built with the iterative use of Coot[73] and Isolde plugin[74] for ChimeraX.[55] Phenix[75] was used for applying symmetry and restraint calculation for lipid molecules. The pore structure of the wtFav (PDBid: 9EYM) was used as the starting model. Each protomer (subunit) in a pore is identical to the rest. This is true for both types of pores. For the octameric RN1-Fav pore, the model was built from Ile 78 to Met 259. In addition to the protein, 6 lipid (sphingomyelin) molecules per protomer (48 in total) were placed in the model. For nonameric RN1-Fav pore, the protein model was built from Ala 79 to Met 259. In addition to the protein, 5 lipid (sphingomyelin) molecules per protomer (45 in total) were placed in the model. Details of data acquisition and refinement statistics are shown in Supplementary Table S1.

The structural models for histones H3.1 and H4 were predicted with AlphaFold 3.[76] As the input, we used histone protein sequences provided by the suppliers.

MinION Experiments

For pore insertion into polymeric membranes, we used empty MinION flow cells provided by Oxford Nanopore Technologies (United Kingdom), the MinION setup, an Oxford Nanopore storage buffer[77] and a 20 kHz sampling frequency. Prior to pore insertion, each flow cell was washed with 1 mL of the storage buffer and inspected by membrane quality control measurements. For pore insertion, 1−10 μL of pore sample with a concentration of 0.015 mg/mL was diluted into a final 1 mL of the storage buffer. Pore insertion was performed by adding 300 μL of diluted pore sample via the sample port and running the MinKNOW pore insertion script. For I/V curve measurements, we used a voltage protocol starting at 0 mV and increasing by ±10 mV steps to reach ±120 mV. Before applying histone proteins to inserted pores, we measured the open pore current at 0 mV (10 s), −50 mV (60−300 s), and +50 mV (20 s). The same voltage protocol (if not stated otherwise) was run after applying 100 μL of (0.5–4 μM) histones diluted in a storage buffer. At the end of the measurement, the cells were washed with 1 mL of the storage buffer and the same voltage protocol was applied again to confirm the removal of histone proteins from the flow cell. If measuring multiple concentrations or mixtures on the same flow cell, the washing step was applied after each measurement.

We used the following histones: H3.1 (Human H3 − WT (3.1), The Histone Source, Colorado State University, USA), H3K9ac (Recombinant Histone H3K9ac (EPL), Active Motif, USA), H3K23ac (Recombinant Histone H3K23ac (EPL), Active Motif, USA), H3Cit (Citrullinated Histone H3 (human, recombinant), Cayman Chemical, USA), and H4 (Human H4, The Histone Source, Colorado State University, USA). The net charge of histones was determined by using the manufacturer-reported sequence as input for the Protpi Protein Tool available at https://www.protpi.ch/Calculator/ProteinTool. The sample purity was confirmed with SDS-PAGE.

MinION Data Analysis

The analysis of data obtained by MinION reads was done by our own MATLAB R2022b (MathWorks, USA) script. Before calculating the mean current for I/V curves and its standard deviation, for a specific pore at a specific voltage, the data were down-sampled 100 times. Signal-to-nose (signal/noise) for each pore was calculated by dividing the pore's mean current at specific voltage by its standard deviation. To analyze the blockade events in the presence of histones, we determined the pores that stayed active along the whole measurement. The open pore currents (at −50 mV) (I_{k0}) for pores were plotted as a histogram for which we employed the Gaussian fit. Pores that were within one standard deviation from the peak of the fit were used for the event detection. All traces were filtered using the Morlet-type wavelet filter with wavelet center frequencies 1 and the wavelets bandwidth 5 kHz and no down sampling was applied. To normalize the data, the control traces and the traces in the presence of histones were divided by the mean open pore current at −50 mV of the control measurement (I_{k0}). The bulk analysis data were calculated by averaging the mean current and its standard deviation (noise) at −50 mV for all pores included in analysis.

To gain the blockade parameters, we used the threshold-based method, where the current had to exceed 4.5 standard deviations above the open pore current standard deviation, and the change had to be at least 5 ms long (the minimal dwell time). For each event, its mean current (blockade amplitude, $I_0 - I_h/I_0$, where I_0 is the relative open pore current at −50 mV and I_h is mean current of the blockade), its standard deviation, and the dwell time were calculated. Data were plotted by MATLAB R2022b and Origin 2018 (OriginLab, USA).

Molecular Dynamics Simulations

Lysenin[51] and the RN1-Fav model obtained from cryo-electron microscopy (PDBid: 9EYP) structures were each positioned into a POPC lipid bilayer using CHARMM-GUI.[78] Both systems were electro-neutralized and immersed in 150 mM NaCl aqueous solution within the simulation box of dimensions 148 Å × 148 Å × 145 Å for lysenin and 149 Å × 149 Å × 119 Å for RN1-Fav. Both systems were energetically minimized and equilibrated during initial 100 ns molecular dynamics runs. All simulations were carried out on GPUs with the CUDA version of the NAMD molecular dynamics software suite.[79] The CHARMM36 force field[80] was used and water was modeled by the TIP3P water model.[81] All equilibration and production simulations used the NPT ensemble in the total simulation time of 300 ns (200 ns production) for each system. Temperature was held constant at 303.15 K using the Langevin thermostat and a dampening constant of 1 ps^{-1}. The pressure was held constant at 1.0 bar. The cutoff for nonbonded interactions was set to 12 Å, and electrostatic interactions were calculated using the Particle Mesh Ewald method (PME). Structural flexibility of the pore is visualized by showing fluctuations of radial distances to the centers of mass of selected residues of each protomer from the pore axis at two rings located in the top (lysenin residues: 44, 46, 48, 93, 95; RN1-Fav residues: 102−105) and the bottom (lysenin residues: 61−65, 76, 77; RN1-Fav residues: 79−85) of each channel (Supporting Information Figure S6e,f).

■ ASSOCIATED CONTENT

Data Availability Statement

The cryo-EM maps of octameric and nonameric RN1-Fav pores were deposited in EMDB (EMD-50061 and EMD-50062). The models were deposited in the Protein Data Bank (9EYP and 9EYQ). Raw movies have been deposited in EMPIAR (EMPIAR-13273).

Supporting Information

The Supporting Information is available free of charge at https://pubs.acs.org/doi/10.1021/acssensors.5c03533.

https://doi.org/10.1021/acssensors.5c03533
ACS Sens. 2026, 11, 2016−2029

Amino acid sequence alignment, insertion of ΔN-Fav constructs into MinION flow cells, data analysis workflow, RN1-Fav structure, separation of octameric and nonameric RN-Fav and RN1-Fav pores by ion-exchange chromatography, properties of RN1-Fav in comparison to lysenin, histone H4 capturing at different voltages, histone H3.1 capturing at different voltages, interaction of FraC pores with H4, open pore current restoration at positive voltage polarity, MinION measurement repeatability for histones H4, H3.1, H3Cit, H3K9ac, and H3K23ac, event analysis workflow, machine learning assisted histone mixture recognition, cryo-electron microscopy data collection, processing, and model validation statistics, statistical analysis of traces. (PDF)

AUTHOR INFORMATION

Corresponding Author

Gregor Anderluh – *Department of Molecular Biology and Nanobiotechnology, National Institute of Chemistry, Ljubljana 1000, Slovenia*; orcid.org/0000-0002-9916-8465; Email: gregor.anderluh@ki.si

Authors

Marija Srnko – *Department of Molecular Biology and Nanobiotechnology, National Institute of Chemistry, Ljubljana 1000, Slovenia*

Gašper Šolinc – *Department of Molecular Biology and Nanobiotechnology, National Institute of Chemistry, Ljubljana 1000, Slovenia*; orcid.org/0000-0001-8243-0781

Ana Crnković – *Department of Molecular Biology and Nanobiotechnology, National Institute of Chemistry, Ljubljana 1000, Slovenia*; orcid.org/0000-0002-0581-1887

Franci Merzel – *Theory Department, National Institute of Chemistry, Ljubljana 1000, Slovenia*

Michael Jordan – *Oxford Nanopore Technologies Plc, Gosling Building, Edmund Halley Road, Oxford Science Park, Oxford OX4 4DQ, UK*

E. Jayne Wallace – *Oxford Nanopore Technologies Plc, Gosling Building, Edmund Halley Road, Oxford Science Park, Oxford OX4 4DQ, UK*

Marjetka Podobnik – *Department of Molecular Biology and Nanobiotechnology, National Institute of Chemistry, Ljubljana 1000, Slovenia*

Complete contact information is available at: https://pubs.acs.org/10.1021/acssensors.5c03533

Author Contributions

The manuscript was written through contributions of all authors. All authors have given approval to the final version of the manuscript.

Funding

This project was funded by the Slovenian Research and Innovation Agency (ARIS) project grants J4-8225, J4-2547, program grant P1-0391, the Marie Skłodowska-Curie grant agreement No. 896849, and Oxford Nanopore Technologies (United Kingdom). Structural characterization of Fav pores was performed at the National Institute of Chemistry Cryo-EM Facility, supported by ARIS infrastructure program IO-0003.

Notes

All authors, apart from Franci Merzel, are listed as inventors on a patent that covers Fav pores and their use in histone sensing. Part of this study was funded by Oxford Nanopore Technologies.

ACKNOWLEDGMENTS

We would also like to thank Tomaž Švigelj and Matija Ruparčič for the help with protein isolations and pore preparations.

REFERENCES

(1) Bayley, H. Nanopore sequencing: from imagination to reality. *Clin. Chem.* **2015**, *61* (1), 25–31.

(2) Crnković, A.; Srnko, M.; Anderluh, G. Biological Nanopores: Engineering on Demand. *Life* **2021**, *11* (1), 27.

(3) Ying, Y.-L.; Hu, Z.-L.; Zhang, S.; Qing, Y.; Fragasso, A.; Maglia, G.; Meller, A.; Bayley, H.; Dekker, C.; Long, Y.-T. Nanopore-based technologies beyond DNA sequencing. *Nat. Nanotechnol.* **2022**, *17* (11), 1136–1146.

(4) Kasianowicz, J. J.; Brandin, E.; Branton, D.; Deamer, D. W. Characterization of individual polynucleotide molecules using a membrane channel. *Proc. Natl. Acad. Sci. U. S. A.* **1996**, *93* (24), 13770–13773.

(5) Jain, M.; Koren, S.; Miga, K. H.; Quick, J.; Rand, A. C.; Sasani, T. A.; Tyson, J. R.; Beggs, A. D.; Dilthey, A. T.; Fiddes, I. T.; Malla, S.; Marriott, H.; Nieto, T.; O'Grady, J.; Olsen, H. E.; Pedersen, B. S.; Rhie, A.; Richardson, H.; Quinlan, A. R.; Snutch, T. P.; Tee, L.; Paten, B.; Phillippy, A. M.; Simpson, J. T.; Loman, N. J.; Loose, M. Nanopore sequencing and assembly of a human genome with ultra-long reads. *Nat. Biotechnol.* **2018**, *36* (4), 338–345.

(6) Alfaro, J. A.; Bohländer, P.; Dai, M.; Filius, M.; Howard, C. J.; van Kooten, X. F.; Ohayon, S.; Pomorski, A.; Schmid, S.; Aksimentiev, A.; Anslyn, E. V.; Bedran, G.; Cao, C.; Chinappi, M.; Coyaud, E.; Dekker, C.; Dittmar, G.; Drachman, N.; Eelkema, R.; Goodlett, D.; Hentz, S.; Kalathiya, U.; Kelleher, N. L.; Kelly, R. T.; Kelman, Z.; Kim, S. H.; Kuster, B.; Rodriguez-Larrea, D.; Lindsay, S.; Maglia, G.; Marcotte, E. M.; Marino, J. P.; Masselon, C.; Mayer, M.; Samaras, P.; Sarthak, K.; Sepiashvili, L.; Stein, D.; Wanunu, M.; Wilhelm, M.; Yin, P.; Meller, A.; Joo, C. The emerging landscape of single-molecule protein sequencing technologies. *Nat. Methods* **2021**, *18* (6), 604–617.

(7) Bonini, A.; Sauciuc, A.; Maglia, G. Engineered nanopores for exopeptidase protein sequencing. *Nat. Methods* **2024**, *21* (1), 16–17.

(8) Sauciuc, A.; Morozzo Della Rocca, B.; Tadema, M. J.; Chinappi, M.; Maglia, G. Translocation of linearized full-length proteins through an engineered nanopore under opposing electrophoretic force. *Nat. Biotechnol.* **2023**, *42*, 1275.

(9) Huang, G.; Willems, K.; Bartelds, M.; van Dorpe, P.; Soskine, M.; Maglia, G. Electro-Osmotic Vortices Promote the Capture of Folded Proteins by PlyAB Nanopores. *Nano Lett.* **2020**, *20* (5), 3819–3827.

(10) Straathof, S.; Di Muccio, G.; Yelleswarapu, M.; Alzate Banguero, M.; Wloka, C.; van der Heide, N. J.; Chinappi, M.; Maglia, G. Protein Sizing with 15 nm Conical Biological Nanopore YaxAB. *ACS Nano* **2023**, *17* (14), 13685–13699.

(11) Rodriguez-Larrea, D.; Bayley, H. Multistep protein unfolding during nanopore translocation. *Nat. Nanotechnol.* **2013**, *8* (4), 288–295.

(12) Zernia, S.; van der Heide, N. J.; Galenkamp, N. S.; Gouridis, G.; Maglia, G. Current Blockades of Proteins inside Nanopores for Real-Time Metabolome Analysis. *ACS Nano* **2020**, *14* (2), 2296–2307.

(13) Wloka, C.; Van Meervelt, V.; van Gelder, D.; Danda, N.; Jager, N.; Williams, C. P.; Maglia, G. Label-Free and Real-Time Detection of Protein Ubiquitination with a Biological Nanopore. *ACS Nano* **2017**, *11* (5), 4387–4394.

(14) Shorkey, S. A.; Du, J.; Pham, R.; Strieter, E. R.; Chen, M. Real-Time and Label-Free Measurement of Deubiquitinase Activity with a MspA Nanopore. *ChemBioChem* **2021**, *22* (17), 2688–2692.

(15) Cao, C.; Magalhaes, P.; Krapp, L. F.; Bada Juarez, J. F.; Mayer, S. F.; Rukes, V.; Chiki, A.; Lashuel, H. A.; Dal Peraro, M. Deep

Learning-Assisted Single-Molecule Detection of Protein Post-translational Modifications with a Biological Nanopore. *ACS Nano* **2023**, *18*, 1504.
(16) Restrepo-Perez, L.; Wong, C. H.; Maglia, G.; Dekker, C.; Joo, C. Label-Free Detection of Post-translational Modifications with a Nanopore. *Nano Lett.* **2019**, *19* (11), 7957–7964.
(17) Nova, I. C.; Ritmejeris, J.; Brinkerhoff, H.; Koenig, T. J. R.; Gundlach, J. H.; Dekker, C. Detection of phosphorylation post-translational modifications along single peptides with nanopores. *Nat. Biotechnol.* **2024**, *42* (5), 710–714.
(18) Ensslen, T.; Sarthak, K.; Aksimentiev, A.; Behrends, J. C. Resolving Isomeric Posttranslational Modifications Using a Biological Nanopore as a Sensor of Molecular Shape. *J. Am. Chem. Soc.* **2022**, *144* (35), 16060–16068.
(19) Zhang, L.; Gardner, M. L.; Jayasinghe, L.; Jordan, M.; Aldana, J.; Burns, N.; Freitas, M. A.; Guo, P. Detection of single peptide with only one amino acid modification via electronic fingerprinting using reengineered durable channel of Phi29 DNA packaging motor. *Biomaterials* **2021**, *276*, No. 121022.
(20) Ouldali, H.; Sarthak, K.; Ensslen, T.; Piguet, F.; Manivet, P.; Pelta, J.; Behrends, J. C.; Aksimentiev, A.; Oukhaled, A. Electrical recognition of the twenty proteinogenic amino acids using an aerolysin nanopore. *Nat. Biotechnol.* **2019**, *38*, 176.
(21) Brinkerhoff, H.; Kang, A. S. W.; Liu, J.; Aksimentiev, A.; Dekker, C. Multiple rereads of single proteins at single−amino acid resolution using nanopores. *Science* **2021**, *374* (6574), 1509–1513.
(22) Wang, J.; Prajapati, J. D.; Gao, F.; Ying, Y.-L.; Kleinekathöfer, U.; Winterhalter, M.; Long, Y.-T. Identification of Single Amino Acid Chiral and Positional Isomers Using an Electrostatically Asymmetric Nanopore. *J. Am. Chem. Soc.* **2022**, *144* (33), 15072–15078.
(23) Abraham Versloot, R. C.; Arias-Orozco, P.; Tadema, M. J.; Rudolfus Lucas, F. L.; Zhao, X.; Marrink, S. J.; Kuipers, O. P.; Maglia, G. Seeing the Invisibles: Detection of Peptide Enantiomers, Diastereomers, and Isobaric Ring Formation in Lanthipeptides Using Nanopores. *J. Am. Chem. Soc.* **2023**, *145* (33), 18355–18365.
(24) Aronson, J. K.; Ferner, R. E. Biomarkers-A General Review. *Curr. Protoc. Pharmacol.* **2017**, *76*, 9.23.1–9.23.17.
(25) Xu, J.; Zhang, X.; Monestier, M.; Esmon, N. L.; Esmon, C. T. Extracellular histones are mediators of death through TLR2 and TLR4 in mouse fatal liver injury. *J. Immunol.* **2011**, *187* (5), 2626–2631.
(26) Szatmary, P.; Huang, W.; Criddle, D.; Tepikin, A.; Sutton, R. Biology, role and therapeutic potential of circulating histones in acute inflammatory disorders. *J. Cell. Mol. Med.* **2018**, *22* (10), 4617–4629.
(27) Chen, R.; Kang, R.; Fan, X. G.; Tang, D. Release and activity of histone in diseases. *Cell Death Dis.* **2014**, *5* (8), No. e1370.
(28) Shimono, K.; Ito, T.; Kamikokuryo, C.; Niiyama, S.; Yamada, S.; Onishi, H.; Yoshihara, H.; Maruyama, I.; Kakihana, Y. Damage-associated molecular patterns and fibrinolysis perturbation are associated with lethal outcomes in traumatic injury. *Thromb. J.* **2023**, *21* (1), 91.
(29) Urban, C. F.; Ermert, D.; Schmid, M.; Abu-Abed, U.; Goosmann, C.; Nacken, W.; Brinkmann, V.; Jungblut, P. R.; Zychlinsky, A. Neutrophil extracellular traps contain calprotectin, a cytosolic protein complex involved in host defense against Candida albicans. *PLOS Pathog.* **2009**, *5* (10), No. e1000639.
(30) Peng, W.; Wu, S.; Wang, W. Correlation of serum citrullinated histone H3 levels with disease activity in patients with rheumatoid arthritis. *Clin. Exp. Rheumatol.* **2023**, *41* (9), 1792–1800.
(31) Van den Ackerveken, P.; Lobbens, A.; Pamart, D.; Kotronoulas, A.; Rommelaere, G.; Eccleston, M.; Herzog, M. Epigenetic profiles of elevated cell free circulating H3.1 nucleosomes as potential biomarkers for non-Hodgkin lymphoma. *Sci. Rep.* **2023**, *13* (1), 16335.
(32) Li, P.; Liang, S.; Wang, L.; Guan, X.; Wang, J.; Gong, P. Predictive Value of Neutrophil Extracellular Trap Components for 28-Day All-Cause Mortality in Patients with Cardiac Arrest: A Pilot Observational Study. *Shock* **2023**, *60* (5), 664–670.
(33) Zhan, X.; Liu, D.; Dong, Y.; Gao, Y.; Xu, X.; Xie, T.; Zhou, H.; Wang, G.; Zhang, H.; Wu, P.; He, X.; Sun, C.; Yao, X.; Xu, Y. Early Changes and Predictive Value of Serum Histone H3 Concentration in Urosepsis: A Prospective Observational Study. *Adv. Ther.* **2022**, *39* (3), 1310–1323.
(34) Waduge, P.; Hu, R.; Bandarkar, P.; Yamazaki, H.; Cressiot, B.; Zhao, Q.; Whitford, P. C.; Wanunu, M. Nanopore-Based Measurements of Protein Size, Fluctuations, and Conformational Changes. *ACS Nano* **2017**, *11* (6), 5706–5716.
(35) Larkin, J.; Henley, R. Y.; Muthukumar, M.; Rosenstein, J. K.; Wanunu, M. High-bandwidth protein analysis using solid-state nanopores. *Biophys. J.* **2014**, *106* (3), 696–704.
(36) Rojko, N.; Dalla Serra, M.; Maček, P.; Anderluh, G. Pore formation by actinoporins, cytolysins from sea anemones. *Biochim. Biophys. Acta* **2016**, *1858* (3), 446–456.
(37) Hong, Q.; Gutierrez-Aguirre, I.; Barlič, A.; Malovrh, P.; Kristan, K.; Podlesek, Z.; Maček, P.; Turk, D.; Gonzalez-Manas, J. M.; Lakey, J. H.; Anderluh, G. Two-step membrane binding by Equinatoxin II, a pore-forming toxin from the sea anemone, involves an exposed aromatic cluster and a flexible helix. *J. Biol. Chem.* **2002**, *277* (44), 41916–41924.
(38) Kristan, K.; Podlesek, Z.; Hojnik, V.; Gutiérrez-Aguirre, I.; Gunčar, G.; Turk, D.; González-Mañas, J. M.; Lakey, J. H.; Maček, P.; Anderluh, G. Pore formation by equinatoxin, a eukaryotic pore-forming toxin, requires a flexible N-terminal region and a stable beta-sandwich. *J. Biol. Chem.* **2004**, *279* (45), 46509–46517.
(39) Kristan, K.; Viero, G.; Maček, P.; Dalla Serra, M.; Anderluh, G. The equinatoxin N-terminus is transferred across planar lipid membranes and helps to stabilize the transmembrane pore. *FEBS J.* **2007**, *274* (2), 539–550No. .
(40) Tanaka, K.; Caaveiro, J. M. M.; Morante, K.; González-Mañas, J. M.; Tsumoto, K. Structural basis for self-assembly of a cytolytic pore lined by protein and lipid. *Nat. Commun.* **2015**, *6*, 6337.
(41) Wloka, C.; Mutter, N. L.; Soskine, M.; Maglia, G. Alpha-Helical Fragaceatoxin C Nanopore Engineered for Double-Stranded and Single-Stranded Nucleic Acid Analysis. *Angew. Chem., Int. Ed. Engl.* **2016**, *55* (40), 12494–12498.
(42) Huang, G.; Voet, A.; Maglia, G. FraC nanopores with adjustable diameter identify the mass of opposite-charge peptides with 44 dalton resolution. *Nat. Commun.* **2019**, *10* (1), 835.
(43) Šolinc, G.; Srnko, M.; Merzel, F.; Crnković, A.; Kozorog, M.; Podobnik, M.; Anderluh, G. Cryo-EM structures of a protein pore reveal a cluster of cholesterol molecules and diverse roles of membrane lipids. *Nat. Commun.* **2025**, *16* (1), 2972.
(44) Soskine, M.; Biesemans, A.; Moeyaert, B.; Cheley, S.; Bayley, H.; Maglia, G. An engineered ClyA nanopore detects folded target proteins by selective external association and pore entry. *Nano Lett.* **2012**, *12* (9), 4895–4900.
(45) Wang, Y.-Q.; Cao, C.; Ying, Y.-L.; Li, S.; Wang, M.-B.; Huang, J.; Long, Y.-T. Rationally Designed Sensing Selectivity and Sensitivity of an Aerolysin Nanopore via Site-Directed Mutagenesis. *ACS Sens.* **2018**, *3* (4), 779–783.
(46) Tejuca, M.; Serra, M. D.; Ferreras, M.; Lanio, M. E.; Menestrina, G. Mechanism of membrane permeabilization by sticholysin I, a cytolysin isolated from the venom of the sea anemone Stichodactyla helianthus. *Biochemistry* **1996**, *35* (47), 14947–14957.
(47) Belmonte, G.; Pederzolli, C.; Maček, P.; Menestrina, G. Pore formation by the sea anemone cytolysin equinatoxin II in red blood cells and model lipid membranes. *J. Membr. Biol.* **1993**, *131* (1), 11–22.
(48) Marchioretto, M.; Podobnik, M.; Dalla Serra, M.; Anderluh, G. What planar lipid membranes tell us about the pore-forming activity of cholesterol-dependent cytolysins. *Biophys. Chem.* **2013**, *182*, 64–70.
(49) Nestorovich, E. M.; Rostovtseva, T. K.; Bezrukov, S. M. Residue Ionization and Ion Transport through OmpF Channels. *Biophys. J.* **2003**, *85* (6), 3718–3729.
(50) Yan, S.; Wang, L.; Du, X.; Zhang, S.; Wang, S.; Cao, J.; Zhang, J.; Jia, W.; Wang, Y.; Zhang, P.; Chen, H.-Y.; Huang, S. Rapid and multiplex preparation of engineered Mycobacterium smegmatis porin A (MspA) nanopores for single molecule sensing and sequencing. *Chem. Sci.* **2021**, *12* (27), 9339–9346.

(51) Podobnik, M.; Savory, P.; Rojko, N.; Kisovec, M.; Wood, N.; Hambley, R.; Pugh, J.; Wallace, E. J.; McNeill, L.; Bruce, M.; Liko, I.; Allison, T. M.; Mehmood, S.; Yilmaz, N.; Kobayashi, T.; Gilbert, R. J. C.; Robinson, C. V.; Jayasinghe, L.; Anderluh, G. Crystal structure of an invertebrate cytolysin pore reveals unique properties and mechanism of assembly. *Nat. Commun.* **2016**, *7*, No. 11598.

(52) Niu, H.; Li, M.-Y.; Ying, Y.-L.; Long, Y.-T. An engineered third electrostatic constriction of aerolysin to manipulate heterogeneously charged peptide transport. *Chem. Sci.* **2022**, *13* (8), 2456–2461.

(53) Versloot, R. C. A.; Straathof, S. A. P.; Stouwie, G.; Tadema, M. J.; Maglia, G. β-Barrel Nanopores with an Acidic-Aromatic Sensing Region Identify Proteinogenic Peptides at Low pH. *ACS Nano* **2022**, *16* (5), 7258–7268.

(54) Moiana, M.; Aranda, F.; de Larranaga, G. A focus on the roles of histones in health and diseases. *Clin. Biochem.* **2021**, *94*, 12–19.

(55) Goddard, T. D.; Huang, C. C.; Meng, E. C.; Pettersen, E. F.; Couch, G. S.; Morris, J. H.; Ferrin, T. E. UCSF ChimeraX: Meeting modern challenges in visualization and analysis. *Protein Sci.* **2018**, *27* (1), 14–25.

(56) Chinappi, M.; Yamaji, M.; Kawano, R.; Cecconi, F. Analytical Model for Particle Capture in Nanopores Elucidates Competition among Electrophoresis, Electroosmosis, and Dielectrophoresis. *ACS Nano* **2020**, *14* (11), 15816–15828.

(57) Tsunaka, Y.; Kajimura, N.; Tate, S.-i.; Morikawa, K. Alteration of the nucleosomal DNA path in the crystal structure of a human nucleosome core particle. *Nucleic Acids Res.* **2005**, *33* (10), 3424–3434.

(58) Lu, N.-F.; Jiang, L.; Zhu, B.; Yang, D.-G.; Zheng, R.-Q.; Shao, J.; Xi, X.-M. Elevated plasma histone H4 level predicts increased risk of mortality in patients with sepsis. *Ann. Palliat. Med.* **2020**, *9* (3), 1084–1091.

(59) Zhang, S.; Cao, Z.; Fan, P.; Sun, W.; Xiao, Y.; Zhang, P.; Wang, Y.; Huang, S. Discrimination of Disaccharide Isomers of Different Glycosidic Linkages Using a Modified MspA Nanopore. *Angew. Chem., Int. Ed.* **2024**, *63* (8), No. e202316766.

(60) Cao, C.; Magalhães, P.; Krapp, L. F.; Bada Juarez, J. F.; Mayer, S. F.; Rukes, V.; Chiki, A.; Lashuel, H. A.; Dal Peraro, M. Deep Learning-Assisted Single-Molecule Detection of Protein Post-translational Modifications with a Biological Nanopore. *ACS Nano* **2024**, *18* (2), 1504–1515.

(61) Demšar, J.; Curk, T.; Erjavec, A.; Gorup, C.; Hočevar, T.; Milutinovič, M.; Možina, M.; Polajnar, M.; Toplak, M.; Starič, A.; Štajdohar, M.; Umek, L.; Žagar, L.; Žnbontar, J.; Žitnik, M.; Zupan, B. Z. Orange: Data Mining Toolbox in Python. *J. Mach. Learn. Res.* **2013**, *14*, 2349–2353.

(62) Yu, L.; Kang, X.; Li, F.; Mehrafrooz, B.; Makhamreh, A.; Fallahi, A.; Foster, J. C.; Aksimentiev, A.; Chen, M.; Wanunu, M. Unidirectional single-file transport of full-length proteins through a nanopore. *Nat. Biotechnol.* **2023**, *41* (8), 1130–1139.

(63) Vreeker, E.; Grünewald, F.; van der Heide, N. J.; Bonini, A.; Marrink, S. J.; Tych, K.; Maglia, G. Nanopore-Functionalized Hybrid Lipid-Block Copolymer Membranes Allow Efficient Single-Molecule Sampling and Stable Sensing of Human Serum. *Adv. Mater.* **2025**, *37* (15), No. 2418462.

(64) Mueller, M.; Grauschopf, U.; Maier, T.; Glockshuber, R.; Ban, N. The structure of a cytolytic alpha-helical toxin pore reveals its assembly mechanism. *Nature* **2009**, *459* (7247), 726–730.

(65) Galenkamp, N. S.; Biesemans, A.; Maglia, G. Directional conformer exchange in dihydrofolate reductase revealed by single-molecule nanopore recordings. *Nat. Chem.* **2020**, *12* (5), 481–488.

(66) Jiang, J.; Li, M.-Y.; Wu, X.-Y.; Ying, Y.-L.; Han, H.-X.; Long, Y.-T. Protein nanopore reveals the renin–angiotensin system crosstalk with single-amino-acid resolution. *Nat. Chem.* **2023**, *15* (4), 578–586.

(67) Martin-Baniandres, P.; Lan, W.-H.; Board, S.; Romero-Ruiz, M.; Garcia-Manyes, S.; Qing, Y.; Bayley, H. Enzyme-less nanopore detection of post-translational modifications within long polypeptides. *Nat. Nanotechnol.* **2023**, *18* (11), 1335–1340.

(68) Pan, B.; Li, Y.; Liu, Y.; Wang, W.; Huang, G.; Ouyang, Y. Circulating CitH3 Is a Reliable Diagnostic and Prognostic Biomarker of Septic Patients in Acute Pancreatitis. *Front. Immunol.* **2021**, *12*, No. 766391.

(69) Maheshwaram, S. K.; Shet, D.; David, S. R.; Lakshminarayana, M. B.; Soni, G. V. Nanopore Sensing of DNA–Histone Complexes on Nucleosome Arrays. *ACS Sens.* **2022**, *7* (12), 3876–3884.

(70) Wang, X.; Shi, Z.; Lu, H.-Y.; Kim, J. J.; Bu, W.; Villalobos, J. A.; Perera, D. N.; Jung, S. Y.; Wang, T.; Grimm, S. L.; Taylor, B. C.; Rajapakshe, K.; Park, H.; Wulfkuhle, J.; Young, N. L.; Li, Y.; Coarfa, C.; Edwards, D. P.; Huang, S. High-throughput profiling of histone post-translational modifications and chromatin modifying proteins by reverse phase protein array. *J. Proteomics* **2022**, *262*, No. 104596.

(71) Poncha, K. F.; Paparella, A. T.; Young, N. L., Unraveling Posttranslational Modification Complexity: Advances in Quantitative Histone Proteoform Mass Spectrometry. *Mass Spectrom. Rev.* **2025**.

(72) Punjani, A.; Rubinstein, J. L.; Fleet, D. J.; Brubaker, M. A. cryoSPARC: algorithms for rapid unsupervised cryo-EM structure determination. *Nat. Methods* **2017**, *14* (3), 290–296.

(73) Emsley, P.; Cowtan, K. Coot: model-building tools for molecular graphics. *Biol. Crystallogr.* **2004**, *60* (12), 2126–2132.

(74) Croll, T. I. ISOLDE: a physically realistic environment for model building into low-resolution electron-density maps. *Biol. Crystallogr.* **2018**, *74* (6), 519–530.

(75) Liebschner, D.; Afonine, P. V.; Baker, M. L.; Bunkóczi, G.; Chen, V. B.; Croll, T. I.; Hintze, B.; Hung, L. W.; Jain, S.; McCoy, A. J.; Moriarty, N. W.; Oeffner, R. D.; Poon, B. K.; Prisant, M. G.; Read, R. J.; Richardson, J. S.; Richardson, D. C.; Sammito, M. D.; Sobolev, O. V.; Stockwell, D. H.; Terwilliger, T. C.; Urzhumtsev, A. G.; Videau, L. L.; Williams, C. J.; Adams, P. D. Macromolecular structure determination using X-rays, neutrons and electrons: recent developments in Phenix. *Biol. Crystallogr.* **2019**, *75* (10), 861–877.

(76) Jumper, J.; Evans, R.; Pritzel, A.; Green, T.; Figurnov, M.; Ronneberger, O.; Tunyasuvunakool, K.; Bates, R.; Žídek, A.; Potapenko, A.; Bridgland, A.; Meyer, C.; Kohl, S. A. A.; Ballard, A. J.; Cowie, A.; Romera-Paredes, B.; Nikolov, S.; Jain, R.; Adler, J.; Back, T.; Petersen, S.; Reiman, D.; Clancy, E.; Zielinski, M.; Steinegger, M.; Pacholska, M.; Berghammer, T.; Bodenstein, S.; Silver, D.; Vinyals, O.; Senior, A. W.; Kavukcuoglu, K.; Kohli, P.; Hassabis, D. Highly accurate protein structure prediction with AlphaFold. *Nature* **2021**, *596* (7873), 583–589.

(77) Cardozo, N.; Zhang, K.; Doroschak, K.; Nguyen, A.; Siddiqui, Z.; Bogard, N.; Strauss, K.; Ceze, L.; Nivala, J. Multiplexed direct detection of barcoded protein reporters on a nanopore array. *Nat. Biotechnol.* **2022**, *40* (1), 42–46.

(78) Lee, J.; Cheng, X.; Swails, J. M.; Yeom, M. S.; Eastman, P. K.; Lemkul, J. A.; Wei, S.; Buckner, J.; Jeong, J. C.; Qi, Y.; Jo, S.; Pande, V. S.; Case, D. A.; Brooks, C. L. 3rd; MacKerell, A. D. Jr.; Klauda, J. B.; Im, W. CHARMM-GUI Input Generator for NAMD, GROMACS, AMBER, OpenMM, and CHARMM/OpenMM Simulations Using the CHARMM36 Additive Force Field. *J. Chem. Theory Comput.* **2016**, *12* (1), 405–413.

(79) Phillips, J. C.; Hardy, D. J.; Maia, J. D. C.; Stone, J. E.; Ribeiro, J. V.; Bernardi, R. C.; Buch, R.; Fiorin, G.; Hénin, J.; Jiang, W.; McGreevy, R.; Melo, M. C. R.; Radak, B. K.; Skeel, R. D.; Singharoy, A.; Wang, Y.; Roux, B.; Aksimentiev, A.; Luthey-Schulten, Z.; Kalé, L. V.; Schulten, K.; Chipot, C.; Tajkhorshid, E. Scalable molecular dynamics on CPU and GPU architectures with NAMD. *J. Chem. Phys.* **2020**, *153* (4), No. 044130.

(80) Klauda, J. B.; Venable, R. M.; Freites, J. A.; O'Connor, J. W.; Tobias, D. J.; Mondragon-Ramirez, C.; Vorobyov, I.; MacKerell, A. D.; Pastor, R. W. Update of the CHARMM All-Atom Additive Force Field for Lipids: Validation on Six Lipid Types. *J. Phys. Chem. B* **2010**, *114* (23), 7830–7843.

(81) Jorgensen, W. L.; Chandrasekhar, J.; Madura, J. D.; Impey, R. W.; Klein, M. L. Comparison of simple potential functions for simulating liquid water. *J. Chem. Phys.* **1983**, *79*, 926–935.

https://doi.org/10.1021/acssensors.5c03533
ACS Sens. 2026, 11, 2016–2029